IOP Publishing Journal of Optics
J. Opt. 21 (2019) 085202 (9pp) https://doi.org/10.1088/2040-8986/ab2967

Orientation and separation controllable dual-vortex passively Q-switched microchip laser

Yue Pan, Mingming Zhang and Jun Dong

Laboratory of Laser and Applied Photonics (LLAP), Department of Electronic Engineering, School of Electronic Science and Engineering, Xiamen University, Xiamen 361005, People's Republic of China

E-mail: jdong@xmu.edu.cn

Received 24 February 2019, revised 14 May 2019
Accepted for publication 12 June 2019
Published 5 July 2019

Abstract

Dual-vortex laser beams have been achieved in a decentered annular beam pumped Nd:YAG/Cr^{4+}:YAG composite crystal passively Q-switched microchip laser (PQSML). The orientation and separation between two holes in dual-vortex lasers have been controlled by adjusting the offset of collimating lens with respect to the optical axis of the pump light from fiber-coupled laser diode. The offset of the collimating lens has nearly negligible effect on the performance of the decentered annular beam pumped dual-vortex Nd:YAG/Cr^{4+}:YAG PQSML. The optical efficiency of 15.5% is achieved for dual-vortex lasers, which is comparable to that for doughnut-shaped vortex laser under normal incident pumping. Pulse width is 3.6 ns and peak power is over 5 kW for dual-vortex lasers with controllable orientation and separation between two holes. The short pulse high peak power dual-vortex lasers with controllable orientation and separation between two holes have potential applications in manipulating microparticles, data storage and quantum information processing.

Keywords: dual-vortex laser, passively Q-switched laser, composite crystal, Nd:YAG, annular beam pumping, decentered Gaussian beam

(Some figures may appear in colour only in the online journal)

1. Introduction

The vortex beam with spiral phase [1, 2] carries the orbital angular momentum and can be widely applied in the fields such as particle manipulation [3–5], material processing [6], quantum information [7], optical imaging [8], and optical communication [9, 10]. The Laguerre–Gaussian (LG) beam, especially the $LG_{0,n}$ mode, has been widely studied as the most common vortex beam in recent years [11–14]. However, some applications of the $LG_{0,n}$ vortex beams are restricted because the $LG_{0,n}$ vortices are characterized with only one hole structure. The realization of the dual-vortex laser beam has attracted great attention [15–18]. A dual-vortex laser beam with unique characteristic of adjustable orientation and separation between two holes offers more flexibility for manipulating particles and information processing. Besides the properties of vortex beams, the orientation and separation between two holes in dual-vortex beams introduce two additional variants for information processing, which will dramatically increase the storage capacity of the optical information when it is applied in optical communication. Meanwhile, dual-vortex beams with variable separation between two holes have been used to trap two metal nanoparticles, and overheating in the two dark regions can be avoided [19].

A variety of technologies have been explored for generating dual-vortex lasers. Brambilla *et al* demonstrated a dual-vortex laser based on a mode superposition method [16]. However, the orientation and separation between two holes cannot be controlled because the amplitudes and phases of two modes are fixed in the laser cavity. Bazhenov *et al* reported a common method for generating a dual-vortex beam using a spatial light modulator, and a Gaussian beam was phase-modulated to carry two phase singularities [20]. However, extra optical components make the laser system complex and the laser performance is restricted because of the low damage threshold of spatial light modulators. Toda *et al* also produced a paired optical vortex generated by the second-harmonic using sub-picosecond pulses [21]. Although the orientation of the paired vortices can be changed, the

separation between two vortices cannot be flexibly adjusted. Recently, direct generation of radial polarization and azimuthal polarization switchable optical vortex beam has been demonstrated in an annular beam pumped Nd:YAG microchip laser [22]. Moreover, various transverse laser modes have been obtained in a Nd:YAG/Cr^{4+}:YAG PQSML pumped with a decentered Gaussian beam [23]. High repetition rate, nanosecond pulsed dual-vortex lasers will dramatically enhance the capacity of data storage and flexibility of manipulating macroparticles. The decentered annular beam, formed by offsetting the collimating lens and focusing with a hollow focus lens, could be an effective method for generating dual-vortex or other multi-singularity vortex arrays in PQSMLs. The decentered annular beam induced absorbed pump power distribution inside the gain medium provides possibities for multi-transverse modes oscillation with controllable phases and amplitudes. However, the mechanism of controlling phases and amplitudes of multimode to form stable two-vortex transverse patterns in a solid-state laser are not clear. Nd:YAG/Cr^{4+}:YAG composite crystals fabricated with thermal bonding technology are potential laser materials for constructing highly efficient PQSMLs with high peak power because the air gap between the laser crystal and the Q-switched crystal is eliminated, and the intra-cavity losses are further reduced [24]. It is an interesting topic for investigating direct generation of dual-vortex lasers with controllable orientation and separation between two holes in a decentered annular beam pumped Nd:YAG/Cr^{4+}:YAG composite crystal PQSML.

In this paper, dual-vortex lasers with controllable orientation and separation between two holes have been demonstrated in a decentered annular beam pumped Nd:YAG/Cr^{4+}:YAG composite crystal PQSML. The orientation and separation between two holes in dual-vortex laser beams can be controlled precisely by adjusting the position of collimating lens. The dual-vortex laser pulses with peak power of 5 kW and pulse width of 3.6 ns have been achieved. The effective saturated inversion populations inside the laser crystal for different positions of collimating lens are key factors for forming dual-vortex laser beams with controllable orientation and separation between two holes.

2. Experiments

Figure 1 shows the experimental schematic for generating dual-vortex laser beams with controllable orientation and separation between two holes in a decentered annular beam pumped Nd:YAG/Cr^{4+}:YAG composite crystal PQSML. The laser material is a composite crystal consisting of a 3-mm thick Nd:YAG crystal and a 0.5-mm thick Cr^{4+}:YAG crystal. The doping concentration of Nd^{3+} ions is 1 at.%. The initial transmission of the Cr^{4+}:YAG saturable absorber is 90%. The aperture of the Nd:YAG/Cr^{4+}:YAG composite crystal is 10 mm in diameter. The measured absorption and emission spectra of the Nd:YAG/Cr^{4+}:YAG composite crystal are shown in figure 2. The absorption spectrum of the Nd:YAG/Cr^{4+}:YAG composite crystal combines the absorption spectrum of the Nd:YAG crystal and Cr^{4+}:YAG crystal together. The absorption spectrum

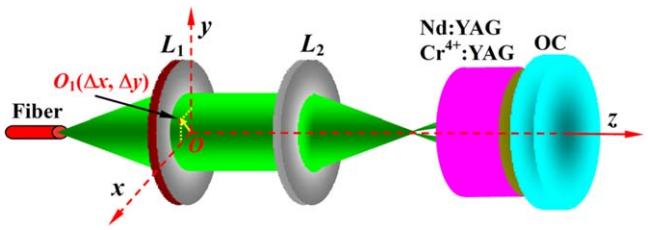

Figure 1. Schematic of a decentered annular beam pumped Nd:YAG/Cr^{4+}:YAG composite crystal PQSML for generating dual-vortex laser beams with controllable orientation and separation between two holes. L_1 is collimating lens. L_2 is hollow focus lens. O is the original coordinate (0,0) when the center of L_1 is coincident with optical axis of pump light. O_1 is the offset coordinate (Δx,Δy) of L_1 with respect to the optical axis of pump light. OC is the output coupler.

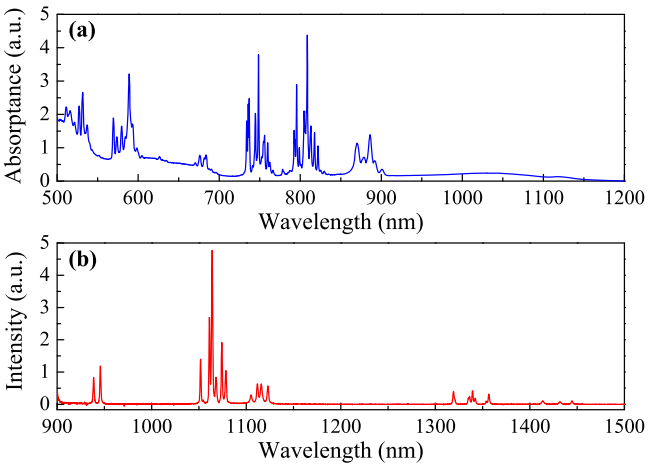

Figure 2. (a) Absorption spectrum and (b) emission spectrum of Nd:YAG/Cr^{4+}:YAG composite crystal at room temperature.

of the Nd:YAG/Cr^{4+}:YAG composite crystal from 750 to 850 nm is similar to that of the Nd:YAG crystal because the Cr^{4+}:YAG crystal has nearly no absorption at this spectral region. The Cr^{4+}:YAG crystal has a broad absorption band from 850 nm to 1200 nm. The emission spectrum of the Nd:YAG/Cr^{4+}:YAG composite crystal is also similar to that of the Nd:YAG crystal, where the strong emission peak is centered at 1064 nm. The Nd:YAG/Cr^{4+}:YAG composite crystal and a plane-parallel output coupling mirror are attached tightly to form the microchip laser resonator. High-reflection at lasing wavelength was coated on the Nd:YAG crystal surface of composite crystal to act as a laser resonator mirror, and anti-reflection at lasing wavelength was coated on the Cr^{4+}:YAG crystal surface of the composite crystal to reduce the intracavity loss. The reflectivity of the plane-parallel output coupler is 70% at 1064 nm. A continuous-wave, fiber coupled laser diode working at 808 nm is employed as the pump source. The pump light from the fiber is collimated with a plano-convex lens (L_1) and focused with a hollow focus lens (L_2) to form an annular pump beam. Both the lenses have the same focal length of 8 mm. The diameter of focus spot was measured to be 170 μm under normal incident pump light on the collimating lens. The decentered annular pump beam is obtained by shifting the L_1 away from the propagation direction of the light from fiber. We placed the

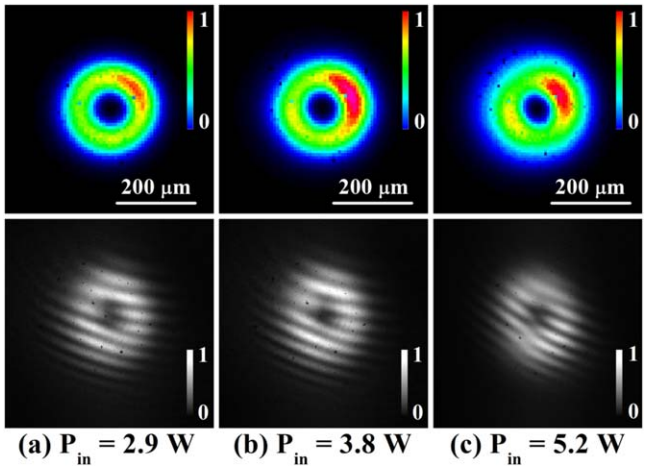

Figure 3. Pump power dependent intensity distribution (upper row) and corresponding interference patterns (low row) of $LG_{0,1}$ doughnut vortices obtained in the Nd:YAG/Cr^{4+}:YAG composite crystal PQSML.

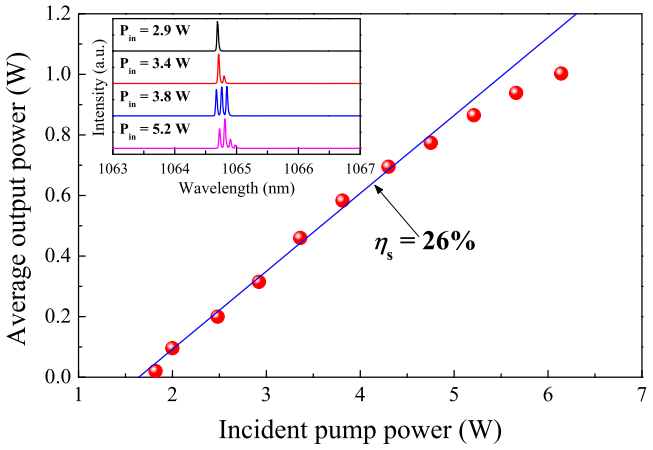

Figure 4. Output power versus incident pump power of annular beam pumped Nd:YAG/Cr^{4+}:YAG composite crystal PQSML for $LG_{0,1}$ doughnut-shaped vortex beam. The inset shows the laser emitting spectra at different incident pump powers.

composite crystal 0.3 mm away from the focus spot of L_2 for achieving good mode matching between pump beam and laser beam. The output laser beam profiles were recorded by a beam profile analyzer (Thorlabs BC106-VIS). The output laser power was measured using a power meter (Thorlabs PM100D). The pulsed laser characteristics were measured with a photo diode and a 1 GHz oscilloscope.

3. Experimental results

When the optical axis of the collimating lens was coincident with the pump light from fiber coupled laser diode, the annular pump beam was normally incident on the composite crystal. The $LG_{0,1}$ doughnut beams were obtained in the Nd:YAG/Cr^{4+}:YAG composite crystal PQSML. Figure 3 shows some intensity distribution profiles of the obtained $LG_{0,1}$ doughnut vortices at different incident pump powers (P_{in}). As P_{in} rises, the output laser transverse profile remains unchanged. However, the intensity of transverse profile increases with P_{in} owing to an increase in the pump power intensity as P_{in} rises. The diameter of the doughnut-shaped beam close to output coupler was measured to be about 220 μm in terms of $1/e^2$ intensity points of the outermost lobe. The size of the singularity of the doughnut-shaped beam is defined as the diameter between maximum intensity of the doughnut beam, which is about 0.7 times of the beam diameter of the doughnut-shaped beam. Therefore, the size of singularity of the doughnut-shaped beam is 150 μm. A Mach–Zehnder interferometer was used to carry out interference experiments to confirm the helical phase nature of the obtained vortices. The measured interference patterns of obtained vortex laser beams with plane-wave reference beam clearly show one fringe splits into two fringes to form a fork-like fringe, and the structure and direction of the fork-like fringe remain nearly unchanged with the increase in the P_{in}. The pump power independent fork-like fringes of the generated $LG_{0,1}$ doughnut beams indicate that the output beam is a vortex beam with one topological charge and constant helicity.

Figure 4 shows the variation of the average output power with respect to the incident pump power. The threshold pump power was measured to be 1.82 W because the large annular pump beam at 0.3 mm away from focus spot was incident on the composite crystal to excite $LG_{0,1}$ vortex laser beam. Therefore, the pump power intensity is lower than that at the focus spot for the same pump power, and high pump power is needed for laser oscillation. A linear increase of the average output power with P_{in} is observed at $P_{in} < 5$ W. The slope efficiency is about 26%. The increased rate of the average output power with P_{in} slows down at $P_{in} > 5$ W. This was caused by the pump power induced intensified thermal effect of the gain medium. The maximum average output power of over 1 W is obtained at P_{in} of 6.14 W, and the corresponding optical efficiency is 16.3%. The optical efficiency of the Nd:YAG/Cr^{4+}:YAG composite crystal PQSML is 50% higher than that achieved in continuous-wave Nd:YAG vortex microchip laser (11.6%) [22]. The achieved optical efficiency of the Nd:YAG/Cr^{4+}:YAG composite crystal PQSML is also higher than that obtained in Cr,Nd:YAG self-Q-switched microchip laser (14% with respect to the incident pump power) [25]. Enhanced performance of Nd:YAG/Cr^{4+}:YAG composite crystal PQSML is attributed to good mode matching between annular pump beam and $LG_{0,1}$ laser beam, and low intracavity loss of composite crystal used in the experiments. The measured laser emitting spectra at different P_{in}s (inset in figure 4) show the laser oscillates around 1064.6 nm and multi-longitudinal mode oscillates depending on P_{in}. The number of the longitudinal modes increases with P_{in}.

Figure 5 gives the variation of repetition rate, pulse width, pulse energy and peak power with P_{in}. The repetition rate increased linearly from 9.25 kHz to 62.25 kHz when the P_{in} increases from 2 W to 6.14 W. According to the theory of the passively Q-switched laser [26], the pulse repetition rate is proportional to the inversion population induced by the pump

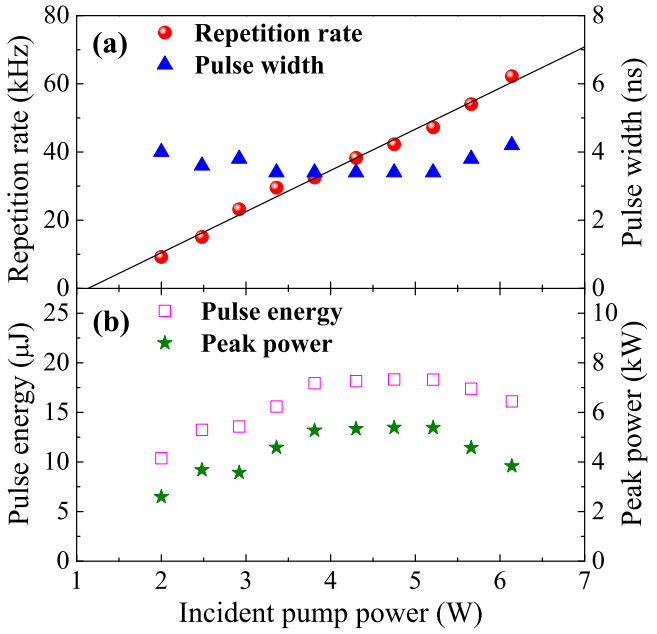

Figure 5. Repetition rate, pulse width, pulse energy and peak power of Nd:YAG/Cr^{4+}:YAG composite crystal PQSML as a function of P_{in}.

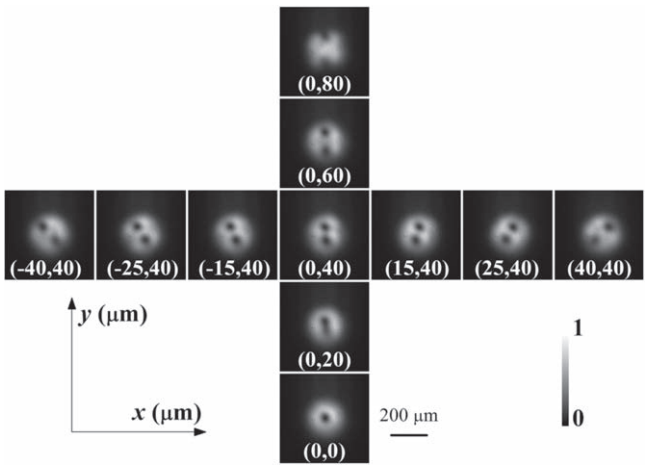

Figure 6. Evolution of dual-vortex laser beam profiles with controllable orientation and separation between two holes at different positions of the collimating lens (Δx, Δy).

power, therefore, the repetition rate increases linearly with the pump power. The pulse width decreases from 4 ns to 3.4 ns when the P_{in} increases from 2 W to 3 W and is kept around 3.4 ns until the P_{in} reaches 5.4 W. The pulse width is broadened with a further increase in the P_{in} due to increase of initial transmission of Cr^{4+}:YAG crystal caused by the strong thermal effect at high pump power. The pulse energy increases with the P_{in} and tends to be a constant of 18 μJ when the P_{in} is higher than 3.5 W. The unchangeable pulse width and pulse energy at high pump power are caused by fully bleaching of the saturable absorber at the high intracavity laser intensity achieved. The pulse width and pulse energy of passively Q-switched microchip laser are determined by the initial transmission of the saturable absorber and cavity length. When the cavity length is set, the pulse width and pulse energy are kept constant when the intracavity laser intensity is high sufficient to beach the saturable absorber. The pulse energy decreases with further increase in the P_{in} owing to the thermal effect induced increase in the initial transmission of the Cr^{4+}:YAG crystal. The peak power exhibits nearly the same tendency as the pulse energy, as shown in figure 5(b). The highest peak power of 5.4 kW is obtained within the pump power range from 3.5 W to 5.2 W, which is about 31 times of that obtained in the Cr,Nd:YAG self-Q-switched microchip vortex laser [25].

Dual-vortex laser beams with controllable orientation and separation between two holes have been obtained in a Nd:YAG/Cr^{4+}:YAG composite crystal PQSML by adjusting the position (Δx,Δy) of L_1 with respect to the pump light propagation direction of the fiber coupled laser diode. When light from the fiber is normally incident on the L_1, the position of the L_1 is labeled as (0, 0). The P_{in} was fixed at 3.8 W, which was one of the pump powers for achieving highest output pulse energy for normally incident pumping condition. When the L_1 was moved away from the pump light propagation direction of fiber coupled laser diode, the output laser beam profile was changed from $LG_{0,1}$-doughnut shape to a dual-vortex profile. The orientation and separation between two holes in the dual-vortex laser beam have been precisely controlled by adjusting the position of the L_1, e.g. moving L_1 from original position O to a random position $O_1(\Delta x,\Delta y)$ along the x-axis and y-axis in figure 1.

Firstly, the L_1 was moved along the y-axis while the position of L_1 along the x-axis was kept unchanged at 0. The offset between the optical axis of L_1 and the optical axis of the pump light from fiber coupled laser diode is Δy. The evolution of dual-vortex laser beam profiles with Δy is shown in figure 6, as depicted in the y-axis. The $LG_{0,1}$-doughnut vortex beam at (0,0) was elongated along the y-axis as Δy increases. The elongated vortex beam eventually changes to a dual-vortex profile when the Δy reaches to 40 μm. The distance between the two holes in the dual-vortex laser profile increases with the Δy, and reaches its maximum when Δy arrives to 80 μm, where both holes have moved to the edge of the laser beam profile. Secondly, the Δy of the L_1 was fixed at 40 μm, the position of the L_1 was moved along the x-axis, and the distance between optical axis of L_1 and the pump beam axis is denoted as Δx. The evolution of dual-vortex laser beam profiles with Δx is shown in the horizontal row of figure 6. As $|\Delta x|$ increases, the dual-vortex laser beam profile is kept, however, the orientation of the dual-vortex laser beam is rotated. The rotation angle increases with $|\Delta x|$ and is kept the same for the same $|\Delta x|$. The results indicate that the orientation and separation between two holes in the dual-vortex laser beams obtained in the Nd:YAG/Cr^{4+}:YAG composite crystal PQSML can be easily controlled by adjusting the position (Δx,Δy) of the L_1.

The phases of dual-vortex beams generated in the Nd:YAG/Cr^{4+}:YAG composite crystal PQSML have been measured by using a Mach–Zehnder interferometer. The output beam was split into two parts with a beam splitter, and a plane wave reference beam was carefully selected with a

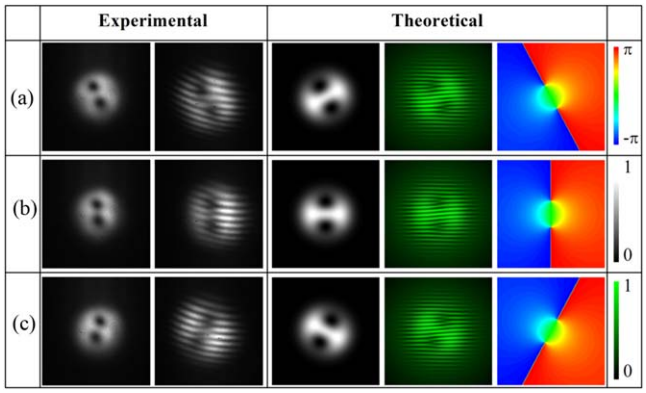

Figure 7. Experimental obtained transverse intensity profiles and interference patterns (1st and 2nd column), and theoretical calculated transverse intensity patterns, interference patterns and phases (3rd, 4th and 5th column) of dual-vortex laser beams at different (Δx, Δy), (a) (−15, 40), (b) (0, 40), (c) (15, 40).

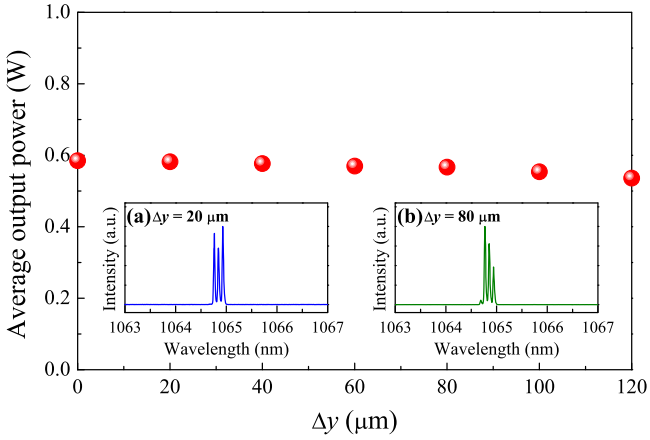

Figure 8. Variation of average output power with Δy for dual-vortex Nd:YAG/Cr^{4+}:YAG composite crystal PQSML under the conditions of $\Delta x = 0$, and $P_{in} = 3.8$ W. Insets (a) and (b) show the typical laser spectra.

tiny aperture. Then the interference patterns were obtained by interfering between plane wave reference beam and the dual-vortex beams. The typical interference fringes of dual-vortex laser beams with different orientations are shown in the 2nd column in figure 7. Two opposite fork-like fringes have been observed for dual-vortex laser beams with different orientations. The two fork-like fringes indicate that the dual-vortex lasers are vortex beams with two opposite topological charges.

The laser performance of dual-vortex PQSML has been measured at different offsets of the collimating lens. The average output power of the dual-vortex lasers as a function of the offset along the *y*-axis (Δy) is shown in figure 8. Under the condition of $P_{in} = 3.8$ W and $\Delta x = 0$, the average output power was 0.59 W at $\Delta y = 0$. The average output power decreases slightly with a further increase of Δy, and it was 0.54 W at $\Delta y = 120$ μm. There is about 8.5% drop of the average output power when the Δy increases from 0 to

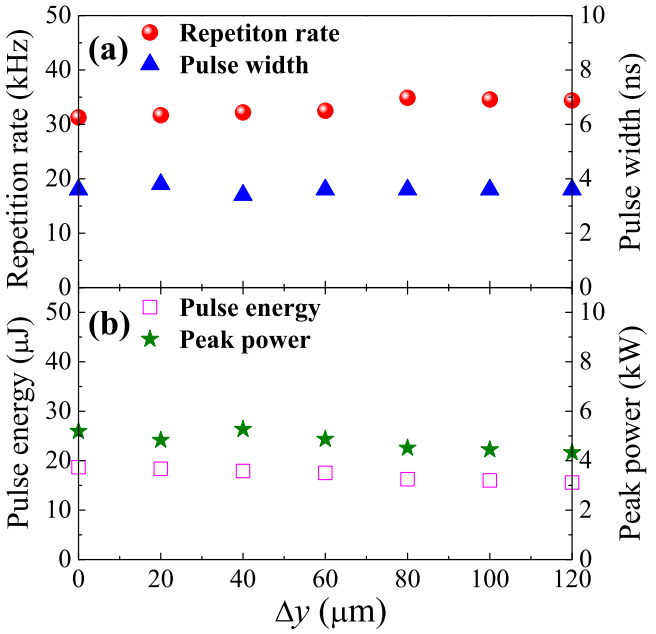

Figure 9. Repetition rate, pulse width, pulse energy and peak power of dual-vortex laser as a function of Δy at the condition of $\Delta x = 0$ and $P_{in} = 3.8$ W.

120 μm. The results indicate that the average output power is nearly independent on the Δy, which provides a flexible method to control the dual-vortex laser with different separation between two holes. The laser emitting spectra at different Δy were measured and found that laser oscillated in three longitudinal modes at $\Delta y < 40$ μm, and oscillated in four longitudinal modes at $\Delta y > 40$ μm.

Figure 9 shows the variation of repetition rate, pulse width, pulse energy and peak power with Δy for dual-vortex laser. The repetition rate nearly keeps about 32 kHz when the Δy increases from 0 to 120 μm. The pulse width is nearly kept a constant of 3.6 ns, independent on the Δy. As the Δy increases from 0 to 120 μm, the pulse energy decreases from 18.9 μJ to 15.6 μJ and the peak power decreases from 5.2 kW to 4.33 kW. The pulse energy and peak power drop about 16.6% when Δy increases from 0 to 120 μm, which is mainly caused by the low pump power intensity induced by the increase of the pump beam area with increase of Δy.

Figure 10 depicts the variation of the average output power of dual-vortex laser with Δx when the Δy is fixed at 40 μm. The average output power decreases from 0.58 W to 0.47 W when the Δx increases from 0 to 80 μm. The further decrease of the average output power with Δx is caused by the decrease of the effective laser beam area which is proportional to the pump beam area with sufficient pump power intensity for laser oscillation. The pump beam area is further enlarged by tilting the incident beam along the *x*-axis, resulting in a further decrease of the pump power intensity under the constant pump power. Therefore, the average output power is further degraded with increase of the offset along the *x*-axis (Δx) under the same pump power. The laser emitting spectra at different Δx were measured and found that laser

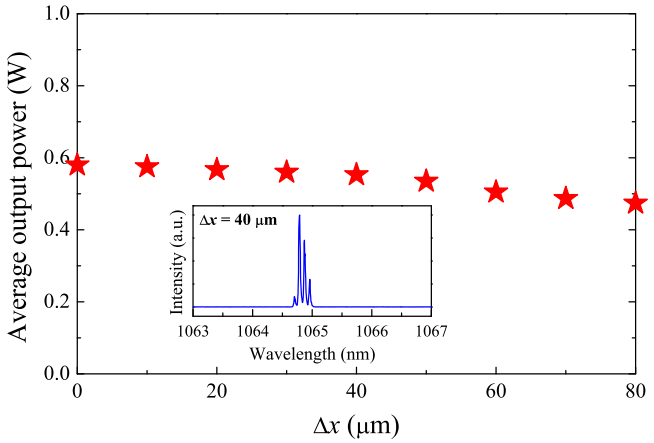

Figure 10. Average output power of dual-vortex PQSML as a function of Δx when the Δy is fixed at 40 μm and P_{in} is set at 3.8 W. The inset shows the typical laser spectrum.

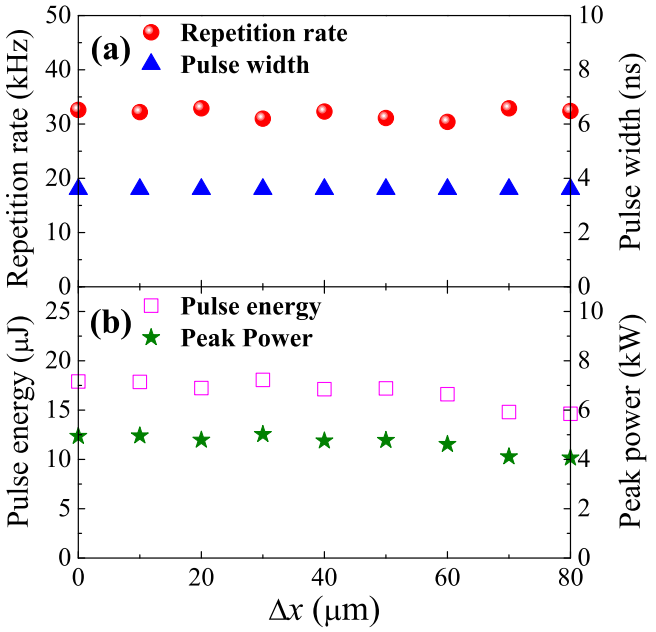

Figure 11. Repetition rate, pulse width, pulse energy and peak power of dual-vortex laser as a function of Δx when the Δy is fixed at 40 μm and P_{in} is 3.8 W.

oscillated in four longitudinal modes for different Δx, as shown in the inset of figure 10.

Figure 11 shows the repetition rate, pulse width, pulse energy and peak power as a function of Δx when the Δy is fixed at 40 μm and P_{in} is set at 3.8 W. The repetition rate is kept around 32 kHz and the pulse width is also kept at 3.6 ns independent on Δx. The pulse energy is about 18 μJ when the Δx is increased to 50 μm and the pulse energy decreases slightly with a further increase in the Δx. There is about 18.3% decrease for the energy when the Δx increases from 0 to 80 μm. The same tendency of the peak power with Δx has been observed. The peak power decreases from 5 kW to 4.1 kW when the Δx increases from 0 to 80 μm. There is about 20% drop of the peak power when the Δx increases from 0 to 80 μm. The decrease of the pulse energy and peak power with Δx is mainly caused by the decrease in the effective laser beam area. When the Δy is fixed at 40 μm, the pump beam area is further enlarged by shifting L_1 along the x-axis, resulting in decrease of the pump power intensity under the same pump power. Therefore, the effective laser beam area is decreased with Δx. The pulse energy and peak power are proportional to the laser beam area, thus the output pulse energy and peak power decrease at large Δx (e.g. $\Delta x > 50$ μm). The performance of dual-vortex lasers at different parameters of Δx and Δy were checked and found that the average output power and pulse characteristics were kept unchanged for over 10 min. Meanwhile, the beam profiles were stable for long term operation. Therefore, stable laser operation was achieved in a dual-vortex passively Q-switched microchip laser.

4. Theoretical analysis and discussion

It is well known that formation of laser mode in a resonator is mainly determined by the inversion population distribution in the gain medium. The hollow focus lens focused annular pump beam used in the laser experiment is similar to a $LG_{0,1}$ beam profile. Therefore, by offsetting the collimating lens, L_1, along the x-axis and y-axis, the decentered annular beams with different tilted angles were obtained. The inversion population inside the gain medium pumped with the decentered annular beam can be expressed as [23, 27]

$$\Delta N(x,y,z) = \frac{2P_{in}\alpha f_a \tau[(-x\sin(\varphi)+y\cos(\varphi))^2 + (-z\sin(\theta)+(x\cos(\varphi)+y\sin(\varphi))\cos(\theta))^2]}{h\nu_p \pi w_p^2 (z\cos(\theta)+(x\cos(\varphi)+y\sin(\varphi))\sin(\theta))} \cdot \exp\left[-2\left(\frac{(-x\sin(\varphi)+y\cos(\varphi))^2 + (-z\sin(\theta)+(x\cos(\varphi)+y\sin(\varphi))\cos(\theta))^2}{w_p^2(z\cos(\theta)+(x\cos(\varphi)+y\sin(\varphi))\sin(\theta))}\right)\cdot\exp(-\alpha z)\right] \quad (1)$$

where P_{in} is the incident pump power, f_a is the fractional equilibrium Boltzmann population in the upper laser level (1 for a four-level system), α and τ are the absorption coefficient and the fluorescence lifetime of the gain medium respectively, h is the Planck constant, ν_p is the frequency of the pump beam, w_p is the pump beam waist, φ indicates the angle between $\Delta x\vec{x} + \Delta y\vec{y}$ and the x-axis, and θ denotes the incident angle of the pump beam with respect to the laser beam axis and is expressed as [23]

$$\theta = \frac{z_1 \Delta d}{f_1 f_2} - \frac{\Delta d}{f_1} \quad (2)$$

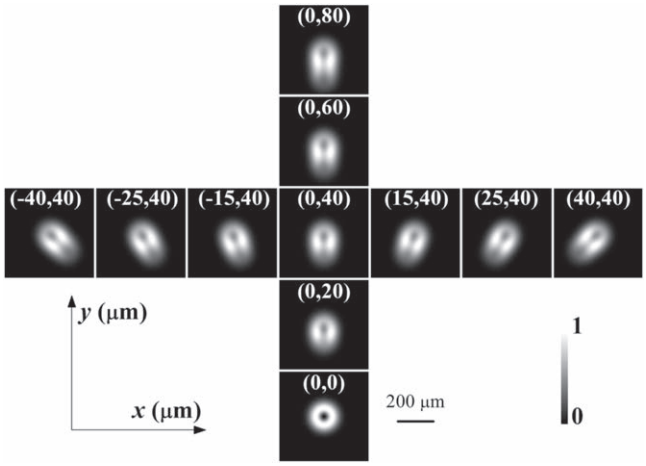

Figure 12. Numerically calculated effective saturated inversion population distributions inside the laser medium in the Nd:YAG/Cr^{4+}:YAG PQSML under decentered annular beam pumping. The position of the collimating lens L_1 is labeled as (Δx, Δy).

where $\Delta d = \sqrt{\Delta x^2 + \Delta y^2}$, f_1 and f_2 are the focal length of the collimating lens L_1 and focus lens L_2, respectively, and z_1 is the distance between the two lenses. By taking into account the intracavity laser intensity, the saturated inversion population can be expressed as

$$N_{sat}(x, y, z) = \frac{\Delta N(x, y, z)}{1 + I(x, y, z)/I_{sat}} \tag{3}$$

where $I(x, y, z)$ is the intracavity laser intensity and I_{sat} is the laser saturation intensity of the gain medium. To reflect the overall effect, we define the effective saturated inversion population to represent the position dependent saturated inversion population distribution in the cavity. The effective saturated inversion population for a laser crystal with length of l is expressed as

$$N_{sat-eff}(x, y) = \int_0^l N_{sat}(x, y, z)dz/l. \tag{4}$$

The effective saturated inversion population distributions in the laser medium at different offsets of L_1 are numerically calculated and are shown in figure 12. The effective saturated inversion population distribution is an annular-shape when the optical axis of the collimating lens is set at original position, e.g. (0,0). The ring-shaped effective saturated inversion population distribution turns to be elongated gradually along the y-axis as the collimating lens is shifted away from the pump light propagation direction emitting from fiber, e.g. $\Delta y > 0$. The effective saturated inversion population distribution is further elongated with increase in Δy, eventually two holes are formed at $\Delta y = 40$ μm, the separation of two holes increases with a further increase in the Δy, as shown in the vertical column in figure 12. When Δy was set at 40 μm, the effective saturated inversion population was calculated at different Δx. The orientation of the effective saturated inversion population distribution was rotated with an increase in the $|\Delta x|$, as shown in the row in figure 12. The change of the effective saturated inversion population distribution with a position of the collimating lens (Δx,Δy) determines the formation of various dual-vortex laser beams in a decentered annular beam pumped Nd:YAG/Cr^{4+}:YAG composite crystal PQSML (figure 6). When the collimating lens is moved to the position (e.g. $\Delta x = 0$, $\Delta y = 80$ μm), the effective saturated inversion population around the edges of the two holes is too weak to support the laser oscillation in the cavity. Therefore, the dual-vortex laser beam tends to disappear and a distorted laser beam profile is observed, as shown in the intensity profile at (0, 80) in figure 6.

The multiple transverse modes oscillation in a laser system depends on the gain achieved to overcome the laser thresholds for different transverse modes, stable multimode transverse patterns are possible when the gains are sufficient to support two or more transverse modes oscillate simultaneously. Therefore, the electrical field of stationary dual-vortex laser can be treated as a superposition of $LG_{1,0}$, $LG_{0,1}$, $LG_{0,-1}$ modes with different weights, which can be described as a linear combination of the three modes [16],

$$E(r, \phi) = E_{1,0}(r, \phi)g_1 + E_{0,1}(r, \phi)|g_2|\ e^{i\theta_2} + E_{0,-1}(r, \phi)|g_3|\ e^{i\theta_3} \tag{5}$$

where $E_{1,0}$, $E_{0,1}$ and $E_{0,-1}$ are the electrical fields of $LG_{1,0}$, $LG_{0,1}$ and $LG_{0,-1}$ modes, g_1, g_2 and g_3 are the weights of amplitudes for $LG_{1,0}$, $LG_{0,1}$ and $LG_{0,-1}$ modes, θ_2, θ_3 are the rotation angles of the $LG_{0,1}$ and $LG_{0,-1}$ modes, satisfying $\theta_2 + \theta_3 = \pi$.

Dual-vortex beam profile was formed theoretically with $g_1 = 1.6$, $g_2 = 1$ and $g_3 = 1$ based on the oscillation of $LG_{1,0}$ and $LG_{0,1}$ modes simultaneously when the $LG_{1,0}$ mode reaches the lasing threshold. The rotation of dual-vortex beam was controlled by adjusting the rotation angles θ_2 and θ_3. The theoretically calculated dual-vortex lasers with different orientations are shown in the 3rd column of figure 7. The theoretically calculated dual-vortex transverse profiles are in good agreement with the experimentally obtained transverse profiles (1st column in figure 7), which indicates the experimentally obtained dual-vortex transverse profiles are superposition of $LG_{1,0}$, $LG_{0,1}$, $LG_{0,-1}$ modes. With the theoretically calculated dual-vortex laser transverse intensity profiles, the interference patterns and phases of the obtained stationary dual-vortex laser with a plane-wave reference beam can be theoretically calculated, as shown in the 4th and 5th columns in figure 7. The theoretically calculated interference patterns indicate two vortices with opposite helical phases oscillate in annular beam pumped Nd:YAG/Cr^{4+}:YAG PQSML. As shown in the 2nd and 4th columns, good agreement is achieved between the theoretically calculated and experimentally obtained interference patterns, which provides strong evidence for an annular beam pumpbed Nd:YAG/Cr^{4+}:YAG PQSML oscillating in two vortices with opposite helical phases.

From experimentally obtained dual-vortex lasers with controllable orientation and separation between two holes and numerically calculated effective saturated inversion population distributions, it is obviously found that dual-vortex laser beams with specified separation between two holes and desired orientation can be obtained by adjusting the position (Δx, Δy) of collimating lens L_1. The separation between two

holes in the dual-vortex laser beam ($\Delta d_{2\text{-hole}}$) obtained in the Nd:YAG/Cr^{4+}:YAG PQSML is proportional to Δd as follows,

$$\Delta d_{2-hole} = 1.75\Delta d. \quad (6)$$

The dual-vortex laser oscillates for Δd with the range from 20 to 113 μm. When the Δd is smaller than 20 μm, the effective saturated inversion population is close to the doughnut-shape and supports the oscillation of doughnut-shaped $LG_{0,1}$ mode. When the collimating lens is moved larger than 80 μm away from the original point along either the x-axis or y-axis, e.g. $\Delta d > 113$ μm, the effective saturated inversion population at the brim of two holes tends to decrease and cannot support dual-vortex laser oscillation because the pump power intensity decreases for a constant pump power as the pump beam area increases.

The angle between the dual-vortex laser beam and the x-axis can be described as,

$$\theta_{2-hole} = \varphi = \arg(\Delta x + i\Delta y). \quad (7)$$

From expression (7), we can obtain the dual-vortex laser beams with arbitrary orientation from 0° to 360° if the Δx and Δy of the collimating lens are precisely controlled.

5. Conclusions

Dual-vortex laser beams have been obtained in a Nd:YAG/Cr^{4+}:YAG composite crystal PQSML pumped with a decentered annular beam. The orientation and separation between two holes in the dual-vortex laser beams have been controlled by moving the collimating lens along the x-axis or y-axis. The performance of the dual-vortex Nd:YAG/Cr^{4+}:YAG composite crystal PQSML is comparable to $LG_{0,1}$-doughnut vortex laser. Average output power of over 1 W has been achieved in $LG_{0,1}$-doughnut vortex Nd:YAG/Cr^{4+}:YAG PQSML, and the optical efficiency is 16.3% with respect to the incident pump power. Average output power of 0.58 W has been obtained in dual-vortex PQSML at incident pump power of 3.8 W, and the optical efficiency is 15.5%. The laser pulses with the pulse energy of 18 μJ, the pulse with of 3.6 ns and the peak power of over 5 kW have been achieved for dual-vortex lasers. High peak power, dual-vortex pulsed lasers with controllable orientation and separation between two holes provide a potential arena for various applications such as micro-particle manipulation, quantum computation, and optical communication.

Acknowledgments

This work was supported by the National Natural Science Foundation of China (61475130 and 61275143), the Program for New Century Excellent Talents in University (NCET-09-0669).

ORCID iDs

Jun Dong https://orcid.org/0000-0001-7072-5435

References

[1] Allen L, Beijersbergen M W, Spreeuw R J C and Woerdman J P 1992 Orbital angular momentum of light and the transformation of Laguerre–Gaussian laser modes *Phys. Rev.* A **45** 8185–9
[2] Yao A M and Padgett M J 2011 Orbital angular momentum: origins, behavior and applications *Adv. Opt. Photonics* **3** 161–204
[3] Grier D G 2003 A revolution in optical manipulation *Nature* **424** 810–6
[4] Franke-Arnold S, Allen L and Padgett M 2008 Advances in optical angular momentum *Laser Photon. Rev.* **2** 299–313
[5] Padgett M and Bowman R 2011 Tweezers with a twist *Nat. Photonics* **5** 343–8
[6] Hamazaki J, Morita R, Chujo K, Kobayashi Y, Tanda S and Omatsu T 2010 Optical-vortex laser ablation *Opt. Express* **18** 2144–51
[7] Molina-Terriza G, Torres J P and Torner L 2007 Twisted photons *Nat. Phys.* **3** 305–10
[8] Jesacher A, Furhapter S, Bernet S and Ritsch-Marte M 2006 Spiral interferogram analysis *J. Opt. Soc. Am.* A **23** 1400–9
[9] Yan Y *et al* 2014 High-capacity millimetre-wave communications with orbital angular momentum multiplexing *Nat. Commun.* **5** 4876
[10] Thide B, Then H, Sjoholm J, Palmer K, Bergman J, Carozzi T D, Istomin Y N, Ibragimov N H and Khamitova R 2007 Utilization of photon orbital angular momentum in the low-frequency radio domain *Phys. Rev. Lett.* **99** 087701
[11] Kim D J and Kim J W 2017 Dual-cavity Nd:YAG laser with Laguerre–Gaussian (LG_{0n}) mode output *Opt. Commun.* **383** 26–30
[12] Ito A, Kozawa Y and Sato S 2010 Generation of hollow scalar and vector beams using a spot-defect mirror *J. Opt. Soc. Am.* A **27** 2072–7
[13] Rueda E, Muneton D, Gomez J A and Lencina A 2013 High-quality optical vortex-beam generation by using a multilevel vortex-producing lens *Opt. Lett.* **38** 3941–4
[14] Chen Y, Fang Z X, Ren Y X, Gong L and Lu R D 2015 Generation and characterization of a perfect vortex beam with a large topological charge through a digital micromirror device *Appl. Opt.* **54** 8030–5
[15] Dong J, Wang X L, Zhang M M, Wang X J and He H S 2018 Structured optical vortices with broadband comb-like optical spectra in Yb:$Y_3Al_5O_{12}$/YVO_4 Raman microchip laser *Appl. Phys. Lett.* **112** 161108
[16] Brambilla M, Battipede F, Lugiato L A, Penna V, Prati F, Tamm C and Weiss C O 1991 Transverse laser patterns. I. Phase singularity crystals *Phys. Rev.* A **43** 5090–113
[17] Rozas D, Law C T and Swartzlander G A 1997 Propagation dynamics of optical vortices *J. Opt. Soc. Am.* B **14** 3054–65
[18] Maleev I D and Swartzlander G A 2003 Composite optical vortices *J. Opt. Soc. Am.* B **20** 1169–76
[19] Dienerowitz M, Mazilu M, Reece P J, Krauss T F and Dholakia K 2008 Optical vortex trap for resonant confinement of metal nanoparticles *Opt. Express* **16** 4991–9
[20] Bazhenov V Y, Soskin M S and Vasnetsov M V 1992 Screw dislocations in light wave-fronts *J. Mod. Opt.* **39** 985–90
[21] Toda Y, Honda S and Morita R 2010 Dynamics of a paired optical vortex generated by second-harmonic generation *Opt. Express* **18** 17796–804

[22] He H S, Chen Z and Dong J 2017 Direct generation of vector vortex beams with switchable radial and azimuthal polarizations in a monolithic Nd:YAG microchip laser *Appl. Phys. Express* **10** 052701

[23] Zhang M M, He H S and Dong J 2017 Decentered Gaussian beam pumped highly efficient passively Q-switched microchip laser for controllable high-order transverse modes *IEEE Photonics J.* **9** 1501214

[24] Miao J G, Wang B S, Peng J Y, Tan H M and Bian H K 2008 Efficient diode-pumped passively Q-switched laser with Nd: YAG/Cr:YAG composite crystal *Opt. Laser Technol.* **40** 137–41

[25] He H S, Chen Z, Li H B and Dong J 2018 Low-threshold, nanosecond, high-repetition-rate vortex pulses with controllable helicity generated in Cr,Nd:YAG self-Q-switched microchip laser *Laser Phys.* **28** 055802

[26] Dong J 2003 Numerical modeling of CW-pumped repetitively passively Q-switched Yb:YAG lasers with Cr:YAG as saturable absorber *Opt. Commun.* **226** 337–44

[27] Dong J, Bai S C, Liu S H, Ueda K I and Kaminskii A A 2016 A high repetition rate passively Q-switched microchip laser for controllable transverse laser modes *J. Opt.* **18** 055205